Unexpected Zero Bias Conductance Peak on the Topological Semimetal Sb(111) with a Single Broken Layer

by a scanning tunneling microscopy and density functional theory study

by

Yau Chuen Yam

B.Sc., The Hong Kong University of Science and Technology, 2014

A THESIS SUBMITTED IN PARTIAL FULFILLMENT OF
THE REQUIREMENTS FOR THE DEGREE OF

MASTER OF SCIENCE

in

The Faculty of Graduate and Postdoctoral Studies

(Physics)

THE UNIVERSITY OF BRITISH COLUMBIA

(Vancouver)

December 2016

Abstract

The signature of the long-sought Majorana fermion from a heterostructure of a superconductor and a topological material is the zero bias conductance peak (ZBCP). Topological semimetal Antimony is a good material in making such heterostructure. Since it is of a bilayer crystal structure, it is expected to be cleaved between bilayers. However, we found that on its cleaved surface there can be steps with step heights corresponding to the intrabilayer distance, indicating that there is a broken layer underneath. The dI/dV spectrum observed using scanning tunneling microscope on these abnormal steps are quite different from the usual Sb spectrum and there is a pronounced ZBCP. Using quasiparticle interference imaging, Landau level spectroscopy and density functional theory (DFT), we found that the ZBCP is originated from the changed band structure through van Hove singularity. This shows that when we try to probe the signature of Majorana fermion in the heterostructure, we need to make sure the ZBCP is not from this trivial origin due to the imperfectness of the topological material.

Preface

The results of this thesis will be going to be submitted to arXiv and possibly Physical Review Letters or Physical Review B in Dec 2016. The scanning tunneling microscope (STM) experiment was carried out in Hoffman lab in Harvard University by the author, Y.-C. Yam, and Y. He and the data was analyzed by the author and P. Chen. The sample used in the experiment was provided by D. Gardner and Y. Lee in MIT. The DFT calculations were performed and interpretated by the author and S. Fang in Harvard University. The Vienna *ab initio* simulation package (VASP) was used for the DFT simulation.

Table of Contents

List of Figures

Acknowledgements

I would like to express my gratitude to my research advisor Professor Jennifer Hoffman for giving me a chance to conduct research in her group and bringing me to work in her lab in Harvard University where I have attended some great classes, met numerous great minds and started to develope my scientific thoughts. I also would like to thank Dr. Yang He and Dr. Zhi-Huai Zhu for their tough and almost sufficient guidance in mastering the control of STM, which make me tougher in working with coworkers.

I am particularly grateful to Shiang Fang in Kaxiras group who has not only assisted me so much with the use of the VASP software, but also shared countless of his computational resources with me, which make many of the calculation involving large slab possible, and demonstrated his research skills to me.

Finally, I have to thank all the others who has given me assitance during my Master program, including but not limited to Dr. Pengcheng Chen, who taught me his tip treament skills in STM, Dr. Mohammad Hamidian, who helped me to start using Matlab for data analysis and explained some STM components to me, Dr. Jhih-Shih You in Demler Group and Adrian Po in Vishwanath Group, with whom I had some very useful and interesting discussions on topological insulators.

Chapter 1

Introduction

Realizing Majorana fermion has become a very hot research topic recent years because of its potential in making qubits for quantum computing [1–3]. It has been proposed that Majorana fermions can be created at the interface between an s-wave superconductor and a topological insulator [4]. The signature of the Majorana fermion [5, 6] would be a zero bias anomaly in the tunneling conductance at the interface. So zero bias peaks (ZBP) observed in the spectrum of a number of experiments [7–10] have drawn much of the attention. However, as pointed out by Liu *et al.* [11] and Cho *et al.* [12], there are many other possible origins of the zero bias anomalies, like the effects of disorder and Kondo effect. We must be very careful in interpreting and verifying the origins of the ZBP. In this thesis, we are going to show that there is an even more unexpected trivial origin of the ZBP, which is just due to a rapid change of sample in the experiment.

Topological semimetal Sb(111) is a very good candidate in making the interface with the superconductor because it has a clean, stable surface and well-defined surface states [13]. Also, due to its simple bilayer structure, it has a much lower critical thickness than other topological materials to decouple surface states on its opposite sides [14]. Moreover, it is less fragile [15] than tetradymite topological insulators, so a superconducting film could be grown on top of it without destroying it. In addition, its semiconducting bulk screens chemical potential variations [16, 17], leading to a more homogeneous surface state, more suited for the superconductor proximity effect study.

However, in our scanning tunneling microscope (STM) experiment, we discovered that a robust ZBP can appear on the cleaved surface of Sb without proximity to superconductivity. Using quasiparticle interference (QPI) imaging, Landau level (LL) spectroscopy in STM and band structure calculation by density functional theory (DFT), we demonstrate that the peak originates from a single layer of Sb, isolated within its ordinary bilayer structure. The isolated layer introduces additional states at negative energy pushing a saddle point up to the Fermi Energy and producing a van Hove singularity at the Fermi level. We thus introduce a cautionary note in the

search for Majorana fermions as ZBP at Sb-superconductor interfaces, and more generally exemplify how easily a trivial state can robustly mimic the long-sought Majorana.

This thesis is organized as follows. Chapter 2 is devoted to provide a review of the principle of STM. Chapter 3 presents an overview of DFT. Our experimental findings, including the ZBP observed on the unusually cleaved Sb surface as well as the QPI and LL measurements, are provided in Chapter 4. The DFT band structure calculations and the explanation to the origin of the ZBP are addressed in Chapter 5. Finally, a summary and conclusion is included in Chapter 6.

Chapter 2

Scanning Tunneling Microscopy

The scanning tunneling microscopy (STM) comprises a metallic tip sitting at the end of a piezo tube scanner which can control the motion of the tip in the x, y, z direction with sub-Angstrom precision with respect to a flat conducting sample surface. The tip is pointing towards the sample at certain height z. When the tip and the sample are in equilibrium, their fermi levels are at the same energy. But when a negative bias voltage -V is applied to the sample, as shown in Fig. 2.1, all the electronics states of the sample would be shifted upwards by $(-e)(-V) = +eV$ with respect to the tip. The electron with higher energy in the sample can tunnel to the empty states of the tip aross the vaccum space, although it does not have enough energy to overcome the vacuum barrier. Classically this is forbidden. But quantum tunneling allows this kind of electron transition, resulting in a current flowing in the tip. Knowing the applied voltage V and the (x,y) location of the tip from the piezo, we can record the current as function of V and location on the sample, which can in turn reflect different properties of the sample.

2.1 Tunneling Current

As addressed in the beginning, if the sample is biased by -V, the energy of the sample states would be raised by eV, as illustrated in Fig. 2.1, and a tunneling current would be created when the electron flow out of the filled states in the sample and into the empty states in the tip. This tunneling current can be calculated by the Fermi Golden Rule.

Consider the current from the sample to the tip for states at energy ϵ with respect to the shifted fermi energy of the sample (i.e. regarding shifted

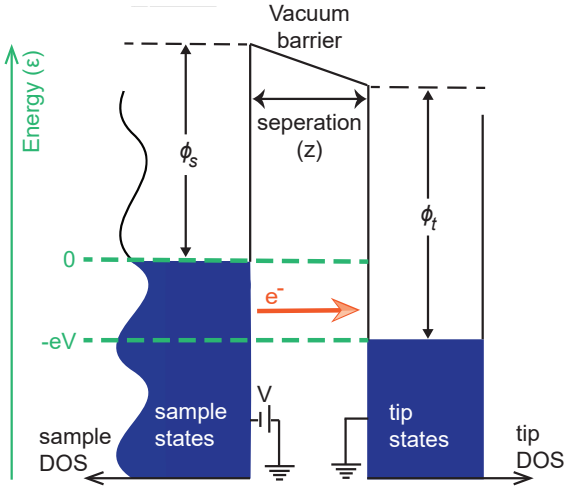

Figure 2.1: **Schematic representation of tip-sample tunneling.** On the sample side, there is a general density of states (DOS) with the filled states in blue. On the tip side, a typical flat density of state is shown with the occupied states in blue. Electron is tunneling from the sample to the tip as indicated by the orange arrow. ϕ_s and ϕ_t are the work fucntions for the sample and the tip respectively.

fermi level of the sample as 0),

$$\begin{aligned} I_{sample\to tip}(\epsilon) &= (-2e)\Gamma_{sample\to tip}(\epsilon) \\ &= (-2e)[\frac{2\pi}{\hbar}|T|^2(\#\text{filled state in sample})(\#\text{empty state in tip})] \\ &= \frac{-4e\pi}{\hbar}|T|^2(n_s(\epsilon)f(\epsilon))(n_t(\epsilon+eV)(1-f(\epsilon+eV)) \end{aligned} \tag{2.1}$$

where in the first line, $\Gamma_{sample\to tip}$ is the transition probability per unit time from the sample to the tip and the '2' take cares of the spin of the electron. In the second line, Fermi Golden rule has been used to express $\Gamma_{sample\to tip}$, with $|T|^2$ being the transition matrix element between the initial filled state and the final empty states. In the third line, $n_s(\epsilon)$ and $n_t(\epsilon)$ are the density of states of the sample and the tip of energy ϵ and f is the occupation number with $f(\epsilon) = \frac{1}{1+e^{\epsilon/k_BT}}$.

To get a form of $|T|^2$, we can regard the vacuum barrier as a a square

barrier and use WKB approximation to find that:

$$|T|^2 = e^{-2\gamma} \tag{2.2}$$

with

$$\gamma = \int_0^z \sqrt{\frac{2m\phi}{\hbar^2}}\, dx = \frac{z}{\hbar}\sqrt{2m\phi} \tag{2.3}$$

where m is the electron mass, $\phi = \frac{1}{2}(\phi_s + \phi_t)$ is the average work function of the tip and the sample and z is the seperation between the tip and the sample.

Please be noted that although the transition from sample to the tip would be dominant, electron could also transit from the tip to the sample at the same time. By symmetry,

$$I_{tip\to sample}(\epsilon) = \frac{-4e\pi}{\hbar}|T|^2(n_s(\epsilon)(1-f(\epsilon)))(n_t(\epsilon+eV)(f(\epsilon+eV)) \tag{2.4}$$

and $|T|^2$ of $I_{tip\to sample}(\epsilon)$ would be the same as that in $I_{tip\to sample}(\epsilon)$. Therefore, the current for states of energy ϵ is

$$\begin{aligned} I(\epsilon) &= I_{sample\to tip}(\epsilon) - I_{tip\to sample}(\epsilon) \\ &= \frac{-4e\pi}{\hbar}|T|^2 n_s(\epsilon)n_t(\epsilon+eV)[f(\epsilon)(1-f(\epsilon+eV)) - (1-f(\epsilon))f(\epsilon+eV)] \end{aligned} \tag{2.5}$$

To find the total current, we have to sum up (or integrate) all the $I(\epsilon)$ from $\epsilon{=}-\infty$ to $+\infty$. But since our measurement was taken at liquid Helium temperature, which is around 4.2K, $k_BT \approx 0.36$ meV, which is sufficiently small compared with our interested energy range of a few hundreds meV. So $f(\epsilon) \approx 1-\theta(\epsilon)$ where θ is the Heavyside step function. Then $f(\epsilon)(1-f(\epsilon+eV)) - (1-f(\epsilon))f(\epsilon+eV) \approx \theta(\epsilon+eV) - \theta(\epsilon) = 1$ if $-eV < \epsilon < 0$ and 0 otherwise. Thus the only concerned energy range is $-eV < \epsilon < 0$.

Therefore, after inserting $|T|^2$ from (2.2) and (2.3) into (2.5) and integrating over energy, the total tunneling current is

$$I = \int_{-\infty}^{\infty} I(\epsilon)\, d\epsilon \approx \frac{-4e\pi}{\hbar}e^{-2\frac{z}{\hbar}\sqrt{2m\phi}}\int_{-eV}^{0} n_s(\epsilon)n_t(\epsilon+eV)\, d\epsilon \tag{2.6}$$

Furthermore, the interested range of V in the Sb experiment was from -300 meV to 300 meV. The tip that we used is made of PtIr which has a flat density of states in this range of energy. So $n_t(\epsilon+eV)$ can be constantly written as $n_t(0)$. Hence, finally, the tunneling current becomes

$$I \approx \frac{-4e\pi}{\hbar}e^{-2\frac{z}{\hbar}\sqrt{2m\phi}}n_t(0)\int_{-eV}^{0} n_s(\epsilon)\, d\epsilon \tag{2.7}$$

2.2 Measurement Modes

2.2.1 Topography

A 'topographic image' showing the structural surface corrugation is the most common measruement that STM can do.

In the topography mode, apart from the constant bias voltage V, the tunneling current will also be set to be fixed. As (2.7) demonstarted, the tunneling current I exponentially depend on the seperation z between the tip and the sample. When there is corrugation on the sample surface, the z-peizo has to extend or retract to maintain the constant seperation z in order to keep the constant current. By monitoring the extension of the z-peizo at different (x,y) location of the sample, the z position of the tip can be infered and from which we can interpret the relative height of the sample surface and map out its 'surface corrugation'.

Clearly, the 'surface corrugation map' here is in fact the contour map of constant current rather than a direct measurement of local height of the surface. In intrepretating the constant current map as a surface corrugation map, we have to make an important assumption that $\int_{-eV}^{0} n_s(\epsilon)\, d\epsilon$ is more or less constant at different location $\vec{r} = (x, y)$. This may not be a too severe simplication generally as long as the entire sample is of the same crystal without abrupt changes in any region and the density of state $n_s(\epsilon)$ does not vary much at different location. But this assumption may be seriously weakened if there is emergent impurities or geometric feature on the surface that can potentially change $n_s(\epsilon)$ severely locally. So we have to pay special attention if we are looking at the topography in these cases.

2.2.2 Density of states

(2.7) let us know that if the tip-sample sepeartion z is fixed, the tunneling current I is proportional to $\int_{-eV}^{0} n_s(\epsilon)\, d\epsilon$, the integrated density of states. To get the density of state, we just need to take its derivative with respect to V. From (2.7),

$$\begin{aligned} I &= I_0 \int_{-eV}^{0} n_s(\epsilon)\, d\epsilon \text{ for some constant } I_0 \\ &= I_0 \int_{-\infty}^{+\infty} n_s(\epsilon)(\theta(\epsilon + eV) - \theta(\epsilon))\, d\epsilon \end{aligned}$$

Taking derivative with respect to V,

$$\begin{aligned}\frac{dI}{dV} &= I_0 \int_{-\infty}^{+\infty} n_s(\epsilon)(\frac{d\theta(\epsilon + eV)}{dV} - 0)\, d\epsilon \\ &= I_0 \int_{-\infty}^{+\infty} n_s(\epsilon)(e\delta(\epsilon + eV))\, d\epsilon \\ &= eI_0 n_s(-eV) \propto n_s(-eV) \end{aligned} \tag{2.8}$$

So theoretically, if the bias voltage is $-V$, taking derivative of the current I with respect to V can tell us the density of states $n_s(-eV)$ at $-eV$. Or in other words, by scanning a bias voltage of V one can find density of state $n_s(eV)$ of energy eV.

However, if we measure $\frac{dI}{dV}$ by taking a derivative numerically, very high energy resolution would be required to prevent errors. So, instead, a standard lockin technique is employed. For the steady bias voltage V applied to the sample, we add an oscillaton $\Delta V = V_{ac}cos(ft)$ to it and a change of ΔI will appear in the tunneling current. (In our experiment, $f = 1.115$kHz.) By measuring the current response ΔI at frequency f and dividing this ΔI by $\Delta V_{rms} = \frac{V_{ac}}{\sqrt{2}}$, the differential conductance $\frac{\Delta I}{\Delta V}$ is obtained and it is proportional to the density of states of the sample as shown by (2.8).

In experiment, $n_s(\epsilon)$ is in general depends on the spatial location $\vec{r}$ on the sample, i.e. $n_s = n_s(\epsilon, \vec{r})$. When we move to a new position, we would fix the seperation z between the tip and the sample by a constant set-point voltage V_{set} and a set-up current I_{set} ('the feedback loop') as explained in the topography mode. Then we will turn off the feedback to allow current I to change with the bias voltage while keeping the other variable, seperation s between tip and sample, constant. After that, we will sweep through a range of bias voltage V with the addition of the voltage oscillation ΔV and record the response of ΔI at each voltage V. In this way, a spectrum of $\frac{\Delta V}{\Delta I}$ at different bias V can be obtained. Lastly, the feedback would be turned on again before moving to the new position.

2.2.3 Linecut and DOS map

Previously, the measurement of the differential conductance spectrum at one spatial point was explained. With the piezo tube scanner, the tip can be moved in the x, y direction with sub-Angstrom precision. So we can acquire the spectra of the sample on a number of points along a line or in a region on the sample surface to form a 'linecut' or 'DOS map' to gain spatial resolution for the density of states.

Chapter 3

Overview of Density Functional Theory

In characterizing the properties of Sb with different terminations, apart from the experimental efforts, we also did some theoretical simulations using density functional theory (DFT), which is an *ab initio* method widely applied to study different properties of tremendous amount of molecules and solid. So this chapter will be devoted to discuss some essential ideas of DFT.

The target of an *ab initio* method is to solve the many-body problem for a solid, which has an enormous number of nuclei and electrons. In particular, we want to solve the Schrödinger equation $\hat{H}\Psi = E\Psi$ where

$$\begin{aligned}\hat{H} = &-\frac{\hbar^2}{2}\sum_i \frac{\nabla^2_{\vec{R}_i}}{M} - \frac{\hbar^2}{2}\sum_i \frac{\nabla^2_{\vec{r}_i}}{m} + \frac{1}{8\pi\varepsilon_0}\sum_{i\neq j}\frac{e^2}{\left|\vec{r}_i - \vec{r}_j\right|} \\ &+\frac{1}{8\pi\varepsilon_0}\sum_{i\neq j}\frac{e^2Z^2}{\left|\vec{R}_i - \vec{R}_j\right|} - \frac{1}{4\pi\varepsilon_0}\sum_{i,j}\frac{e^2Z}{\left|\vec{R}_i - \vec{r}_j\right|}\end{aligned} \tag{3.1}$$

in which $\vec{R}_i$ and $\vec{r}_i$ are the position of the nucleus of mass M and electron of mass m respectively and Z is the number of electron contributed by each nucleus. The first and second term of (3.1) give the kinetic energy of the nuclei and the electron. The thrid and fourth term are the electron-electron and nucleus-nucleus repulsions while the last term is the Coulomb interaction between the electrons and the nuclei.

If there are N nuclei (and thus NZ electrons), there will be 3(N+ZN) degrees of freedom. It is well known that there would be no analytical solution for Ψ if there is more than one particle, not to mention that N is typically in the order of 10^{23} in a condensed matter system. Approximations must be taken in order to make it possible to solve for such system.

3.1 Born-Oppenheimer Approximation

Since the masses of the nuclei are much larger than that of the electrons, they would move much slower than the electrons. We can well assume those nuclei are not moving at all and consider only the motions of electrons. In other words, we can drop the first term of (3.1) which concerns the kinetic energy of the nuclei. Also, since the nucleus-nucleus repulsion term is just a constant in the system, it can be ignored as well. Now we are left with

$$\hat{H} = -\frac{\hbar^2}{2}\sum_i \frac{\nabla^2_{\vec{r}_i}}{m} + \frac{1}{8\pi\varepsilon_0}\sum_{i\neq j}\frac{e^2}{\left|\vec{r}_i - \vec{r}_j\right|} - \frac{1}{4\pi\varepsilon_0}\sum_{i,j}\frac{e^2 Z}{\left|\vec{R}_i - \vec{r}_j\right|} \tag{3.2}$$

which is in the form of $\hat{H} = \hat{T} + \hat{V}_{ee} + \hat{V}_{ext}$ and the scenario of problem becomes a number of negatively charged electrons, with repulsion among themselves resulting in the repulsive potential $\hat{V}_{ee}$, moving in the static postive external potential $\hat{V}_{ext}$ created by the nuclei. In this way, we can greatly reduce 3N degrees of freedom in the problem. This is known as the Born-Oppenheimer Approximation.

3.2 Two Hohenberg-Kohn Theorems

Although the dimensions of the problems have been largely reduced after applying the Born-Oppenherimer Approximation, the many-body Schrödinger equation remains to be unsolvable because its dimension is still as high as 3NZ where N is of orders 10^{23}. There are two ways to further simplify the problem. One is to look for a simpler effective Hamiltonians which can capture the essential physics without directly working with the full Hamiltonian (3.2). Examples of this approach is the Hatree-Fock theory. Another way to tackle this problem is to reformulate the problem so that the full Hamiltonain (3.2) can be retained. This is the approach that DFT has taken.

Suppose the ground state of the system is $\Psi_0(\vec{r}_1, \ldots, \vec{r}_{NZ})$ with 3NZ degree of freedom. The spirit of DFT is that instead of dealing directly with this $\Psi_0(\vec{r}_1, \ldots, \vec{r}_{NZ})$, we could look at the ground state electron density $n_0(\vec{r})$ with only 3 degree of freedom (corresponding to the spatial directions x, y and z). Although intuitively the density seems to contain less information than the wave function does, it is not the case as justified by the two Hohanberg-Kohn Theorems [18].

3.2.1 The First Hohenberg-Kohn theorem

The first Hohenberg-Kohn Theorem stated that the ground state electron density n_0 can uniquely determine the external potential $V_{ext}(\vec{r})$ and thus the Hamiltonian $\hat{H}$. Since the Schrödinger equation with an unique Hamiltonian would yield an unique ground state wave function, the density would contain as much information as the wave function does. The consequence of this would be that we can write down any observable $\hat{O}$ of the system as a functional of the ground state electron density $n_0(\vec{r})$, i.e. $\langle\Psi|\hat{O}|\Psi\rangle = O[n_0(\vec{r})]$. This is where the name 'Density Funtional Theory' from.

This theorem can be proved by contradiction. Assume there are two different external potentials, $V_{ext}(\vec{r})$ and $V'_{ext}(\vec{r})$ giving rise to two different Hamiltonain, $H(\vec{r})$ and $H'(\vec{r})$, corresponding to the same ground state electron density $n_0(\vec{r})$. Let Ψ_0 and Ψ'_0 be the ground states of $\hat{H}$ and $\hat{H}'$ and E_0 and E'_0 be the corresponding ground state energy, i.e. $E_0 = \langle\Psi_0|\hat{H}|\Psi_0\rangle$ and $E'_0 = \langle\Psi'_0|\hat{H}'|\Psi'_0\rangle$. By variatonal principle,

$$\begin{aligned} E_0 < \langle\Psi'_0|\hat{H}|\Psi'_0\rangle &= \langle\Psi'_0|(\hat{H} - V_{ext}(\vec{r}) + V'_{ext}(\vec{r})) + V_{ext}(\vec{r}) - V'_{ext}(\vec{r})|\Psi'_0\rangle \\ &= \langle\Psi'_0|\hat{H}' + V_{ext}(\vec{r}) - V'_{ext}(\vec{r})|\Psi'_0\rangle \\ &= \langle\Psi'_0|\hat{H}'|\Psi'_0\rangle + \langle\Psi'_0|V_{ext}(\vec{r}) - V'_{ext}(\vec{r})|\Psi'_0\rangle \\ &= E'_0 + \langle\Psi'_0|V_{ext}(\vec{r}) - V'_{ext}(\vec{r})|\Psi'_0\rangle \\ &= E'_0 + \int n_0(\vec{r})[V_{ext}(\vec{r}) - V'_{ext}(\vec{r})]\,dr \end{aligned} \tag{3.3}$$

Similarly,

$$E'_0 < \langle\Psi_0|\hat{H}'|\Psi_0\rangle = E_0 + \int n_0(\vec{r})[V'_{ext}(\vec{r}) - V_{ext}(\vec{r})]\,dr \tag{3.4}$$

Summing (3.3) and (3.4),

$$\begin{aligned} E_0 + E'_0 &< E'_0 + E_0 + \int n_0(\vec{r})[V_{ext}(\vec{r}) - V'_{ext}(\vec{r})] + n_0(\vec{r})[V'_{ext}(\vec{r}) - V_{ext}(\vec{r})]\,dr \\ &= E'_0 + E_0 + \int n_0(\vec{r})[V_{ext}(\vec{r}) - V'_{ext}(\vec{r}) + V'_{ext}(\vec{r}) - V_{ext}(\vec{r})]\,dr \\ &= E'_0 + E_0 + 0 \\ &= E_0 + E'_0 \end{aligned} \tag{3.5}$$

The relation of $E_0 + E'_0 < E_0 + E'_0$ in (3.5) is certainly an absurb. Therefore the assumption that different external potentials V_{ext} can have the same electron density n_0 is incorrect and we can conclude that there is a one-to-one correspondence between the ground state electron density n_0 and the external potential V_{ext}.

3.2.2 The Second Hohenberg-Kohn theorem

The second Hohenberg-Kohn theorem reformulates the variational principle in terms of electron density.

The conventional variational principle states in terms of wave function that $\langle\Psi_t|\hat{H}|\Psi_t\rangle \geq E_0$ for any trial state Ψ_t and a general Hamiltonian $\hat{H}$ with ground state energy E_0. By the First Hohenberg-Kohn theorem, the ground state density n_0 can take the place of the wave function Ψ_0 and fully describe the ground state. So even the wave function Ψ itself can be written in terms of the electron density n. In other words, there is a functional $\Psi[n(\vec{r})]$ mapping $n(\vec{r})$ to $\Psi(\vec{r})$. Similarly, the observable ground state energy E_0 can be expressed as a functional of density such that $E_0 = E[n_0]$. In this way, we can completely work with the electron density for the variational principle. So instead of using the trial wavefunction Ψ_t, if we are looking at any trial density n_t, the variational would become $E[n_t(\vec{r})] \geq E_0$.

This theorem implies that in order to find the true ground state density, we can look for the possible trial density n_t which can minimize the energy $E[n_t(\vec{r})]$.

3.3 The Kohn-Sham method

3.3.1 A practical scheme to find the ground state density

Although the Hohenberg-Kohn theorems present a formalism of denisty functional theory in terms of electron density, it does not provide a practical procedure in finding a ground state density. The Kohn-Sham method[19] going to be discussed in this section would fill the gap and offer a recipe to find the ground state density in a self-consistent manner. Until now, the Kohn-Sham method remains to be the only practical tool in implemetating DFT and any DFT calculation would imply that the this method has been used.

The original full interacting system is very difficult to be solved because the electron-electron interaction couples the differential equations together. So the spirit of the Kohn-Sham method is that rather than dealing with this full interacting system, we could design and work with a reference non-interacting system with the same ground electron density. Since this reference system is non-interacting, it would be reduced to the Schrödinger-like *single-particle* equations which is much easier to be solved.

So how do we find such non-interacting reference system? The bad news is that we do not know the exact way to do this. All we can do is group all

unknown terms together into a term called exchange-correlation energy and make sensible approximation to this term.

In the original interacting system, the total energy functional $E[n(\vec{r})]$ of the electron density $n(\vec{r})$ can be written as a sum of the kinetic energy term $T[n(\vec{r})]$, the electron-electron potential energy term $U_{ee}[n(\vec{r})]$ and the external potential energy term $U_{ext}[n(\vec{r})] = \int V(\vec{r})n(\vec{r})\,d\vec{r}$, i.e.

$$E[n(\vec{r})] = T[n(\vec{r})] + U_{ee}[n(\vec{r})] + U_{ext}[n(\vec{r})] \tag{3.6}$$

In the above equation, $U_{ee}[n(\vec{r})]$ can actually be broken into 2 parts, namely $U_{ee}[n(\vec{r})] = U_H[n(\vec{r})] + U_{ex}[n(\vec{r})]$ where $U_H[n(\vec{r})] = \frac{1}{2}\int \frac{e^2}{4\pi\epsilon_0}\frac{n(\vec{r})n(\vec{r}')}{|\vec{r}-\vec{r}'|}\,d\vec{r}\,d\vec{r}'$ is the classical part concerning the Coulomb repulsions between electrons, which is also known as the Hartree-Fock term, and $U_{ex}[n(\vec{r})]$ accounts for the 'exchange energy' arising from the many-body effect whose form is unknown. Also, $T[n(\vec{r})]$ can also be written as $T[n(\vec{r})] = T_s[n(\vec{r})] + T_c[n(\vec{r})]$ where $T_s[n(\vec{r})]$ is going to be the kinetic energy of the non-interacting reference system, which is the sum of *single-particle* kinetic energy of all electrons in the reference system, and $T_c[n(\vec{r})]$, called the 'correlation energy', is the difference of kinetic energy between the non-interacting reference system and true kinetic energy in the interacting system, which is also orginated from the many-body effect and whose form is unknown. The two unknown functionals, $U_{ex}[n(\vec{r})]$ and $T_c[n(\vec{r})]$, can be put together into the co-called exchange-correlation energy functional $E_{xc}[n(\vec{r})]$. The above statemens can be summarised as follows:

$$\begin{aligned} E[n(\vec{r})] &= T_s[n(\vec{r})] + T_c[n(\vec{r})] + U_H[n(\vec{r})] + U_{ex}[n(\vec{r})] + U_{ext}[n(\vec{r})] \\ &= T_s[n(\vec{r})] + U_H[n(\vec{r})] + U_{ext}[n(\vec{r})] + (T_c[n(\vec{r})] + U_{ex}[n(\vec{r})]) \\ &= T_s[n(\vec{r})] + \frac{1}{2}\int \frac{e^2}{4\pi\epsilon_0}\frac{n(\vec{r})n(\vec{r}')}{|\vec{r}-\vec{r}'|}\,d\vec{r}\,d\vec{r}' + \int V(\vec{r})n(\vec{r})\,d\vec{r} + E_{xc}[n(\vec{r})] \end{aligned} \tag{3.7}$$

All we have done above is just rearranging terms of the original system and it is still not useful yet. But now all the unknown many-body parts has been group into a single term. All other terms can be easily decoupled into a *single-particle* operator form by taking a functional derivative of with respect to $n(\vec{r})$. So, we can write down the *single-particle* Hamiltonian for the i^{th} electron, after taking the functional derivative of (3.7),

$$\hat{H}_{KS} = -\frac{\hbar^2}{2m}\vec{\nabla}_i{}^2 + \int \frac{e^2}{4\pi\epsilon_0}\frac{n(\vec{r}')}{|\vec{r}-\vec{r}'|}\,d\vec{r}' + V + V_{xc}[n(\vec{r})] \tag{3.8}$$

where the exchange-correlation potential $V_{xc}[n(\vec{r})] = \frac{\delta E_{xc}[n(\vec{r})]}{\delta n(\vec{r})}$. $\hat{H}_{KS}$ defined in (3.8) is the reference system that we are looking for. It is the Hamiltonian for a single non-interacting classical electron, subjected to two external potentials V and V_{xc}. Assuming V_{xc} is known, we can easily solve the well-studied Schrödinger-like *single-particle* equation

$$\hat{H}_{KS}\phi_i = E_i\phi_i \tag{3.9}$$

for the N lowest-energy wavefunction ϕ_i, if there are N electrons in the original system, and we can construct the ground state electron density by

$$n(\vec{r}) = \sum_{n=1}^{N} \phi_i^*(\vec{r})\phi_i(\vec{r}) \tag{3.10}$$

With this Kohn-Sham method, to find the ground state density, we can not only get around the problem of dealing with orginal coupled interacting differential equations system, but we even do not have to even make use of the second Hohenberg-Kohn theorem and we just have to solve the familiar single-particle Schrödinger equation.

However, $\hat{H}_{KS}$ is actually depending on the electron density $n(\vec{r})$, which in turn depends on the wavefunction ϕ_i that we are trying to solve for. So we need to solve (3.9) self-consistently with the following scheme:

1. Make an initial guess of density $n_i(\vec{r})$
2. Construct the $\hat{H}_{KS}$
3. Solve for the N lowest state ϕ_i
4. Calculate the corresponding density $n_f(\vec{r})$ by $n(\vec{r}) = \sum_{n=1}^{N} \phi_i^*(\vec{r})\phi_i(\vec{r})$
5. If $n_f(\vec{r}) \neq n_i(\vec{r})$, use $n_f(\vec{r})$ as an input to construct $\hat{H}_{KS}$ and repeat 2 to 4 until the input and output density are equal (up to a threshold).

In the above procedure, we have assumed that the nuclei are static. If we allow them to change position after we have found the self-consistent electron density in each static setting, we can look for the position of nuclei which can minimize the energy of the system. This is so called the crystal relaxation. The iterative process can be extended as follows for this purpose:

1. Assume a fixed configuration for nuclei position
2. Calculate the electron ground state with the above self-consistent iteration scheme

3. Calculate net forces on the nuclei by the Hellmann-Feynman theorem.

4. Move the nuclei to the new position and repeat the above process until the forces on them are minimized

3.3.2 Approximation of the exchange-correlation functional

The above methods are looking good. However, please be reminded that they are based on the assumption that we know the form of the exchange correlation functional $V_{xc}[n(\vec{r})]$ in (3.8) such that we have a known $\hat{H}_{KS}$ to solve for. So before we could apply the mentioned methods, we need to first approximate the form of $V_{xc}[n(\vec{r})]$ in justified ways. This leads to an important remarks - researchers have been complaining that experimental measurements can be quite different from what DFT calculated. In DFT we are actually calculating the ground state of the non-interacting Kohn Sham reference system, but not exactly the system of interacting electrons directly. Whether electronic structure and band structure from DFT is physical really depends on how good the approxmation is. There are a number of ways to do the approximation as illustrated in the following. In fact there is still much ongoing efforts on obtaining better forms of $V_{xc}[n(\vec{r})]$.

The most basic and widely used approximation is called the Local Density Approximation (LDA). The form of $V_{xc}[n(\vec{r})]$ from LDA is:

$$V_{xc}[n(\vec{r})] = \int n(\vec{r})\epsilon_{xc}(n(\vec{r}))\, d\vec{r} \tag{3.11}$$

which only depends on the local electron density at the spatial points. $\epsilon_{xc}(n(\vec{r}))$ is the exchange correlation energy for an uniform electron gas system which can be determined numerical methods[20]. This approximation is reasonable because we can divide the whole material into many very small volumes which only has an uniform electron density within themselves. Because of this, we can foresee that LDA would work well for systems with spatially slowly varying density.

An improvement on LDA would be making $V_{xc}[n(\vec{r})]$ depends not only on local electron density $n(\vec{r})$, but also depends on its relation with its neighbor density, i.e. the local gradient of the electron density $\nabla n(\vec{r})$, so that systems with more rapidly varying electron density in space can be treated more accurately. The form of $V_{xc}[n(\vec{r})]$ would thus be:

$$V_{xc}[n(\vec{r})] = \int f(n(\vec{r}), \nabla n(\vec{r}))\, d\vec{r} \tag{3.12}$$

This slightly more general method is called the Generalized Gradient Approximation (GGA). Unlike LDA, which has a uniform electron gas system to be a reference system in determining $\epsilon_{xc}(n(\vec{r}))$, there is no such reference system for GGA to uniquely determine $f(n(\vec{r}), \nabla n(\vec{r}))$. As a results, different versions of GGA exists. Most of them would contain free parameters that need to be fixed by experimental data, making GGA is not strictly an *ab intio* method. However, there is a few forms of GGA that do not have such free parameters, like Perdew-Burke-Ernzerhof (PBE)[21] functional that we have employed in our DFT calculation on the Sb project.

3.4 Pseudopotential to simplify actual computation

Now we have every element for implementing DFT and we can carry calculation using the scheme suggested by the Kohn-Sham method outlined before. In solving the periodic Hamiltonian system, the eigenfunction, by the Bloch theorem, would be:

$$\Psi^n_{\vec{k}}(\vec{r}) = u^n_{\vec{k}}(\vec{r}) e^{i\vec{k}\cdot\vec{r}} \tag{3.13}$$

where n is the band index, $\vec{k}$ is the reciprocal vector in the first Brillouin zone and $u^n_{\vec{k}}(\vec{r})$ is a periodic function with the same periodicity as the lattice, i.e. $u^n_{\vec{k}}(\vec{r}) = \sum_{\vec{K}} c^{n,\vec{k}}_{\vec{K}} e^{i\vec{K}\cdot\vec{r}}$ with $\vec{K}$ being the crystal momentum. So,

$$\begin{aligned} \Psi^n_{\vec{k}}(\vec{r}) &= (\sum_{\vec{K}} c^{n,\vec{k}}_{\vec{K}} e^{i\vec{K}\cdot\vec{r}}) e^{i\vec{k}\cdot\vec{r}} \\ &= \sum_{\vec{K}} c^{n,\vec{k}}_{\vec{K}} e^{i(\vec{k}+\vec{K})\cdot\vec{r}} \end{aligned} \tag{3.14}$$

Now $\Psi^n_{\vec{k}}(\vec{r})$ is expressed in the basis of $e^{i(\vec{k}+\vec{K})\cdot\vec{r}}$, the so-called 'plane wave basis'. This is an infinite basis set because there are infinitely many $\vec{K}$. But practically, the more $\vec{K}$ included, the longer is the computation time. So a cut-off should be set at certain $\vec{K}_{max}$, i.e. we should consider only $\vec{K} < \vec{K}_{max}$, where $\vec{K}_{max}$ can be seen to relate to a cut-off energy E_{cut} by $E_{cut} \sim \frac{\hbar^2 \vec{K}^2_{max}}{2m}$.

Actually, the highly oscillating component of the wave function with high energy only come from the region very close to the nucleus where the potential is very negative, as shown in the left panel of Fig. 3.1. Therefore there are two simplications that we can make.

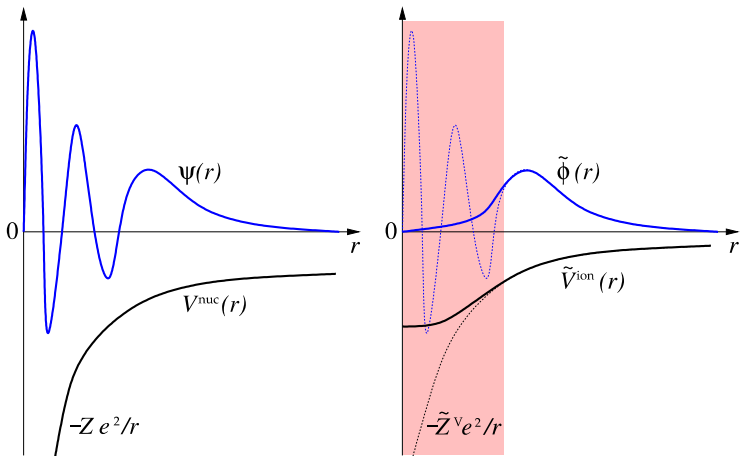

Figure 3.1: **Schematic representation of nucleus potential and pseudopotential.** Left panel is showing the valence electron wavefunction Ψ in the nucleus potential $\tilde{V}^{nuc}$. Right panel is showing the valence electron (pseudo-)wavefunction ϕ in the pseudopotential $\tilde{V}^{ion}$ which matches the original nuclues potential outside the red region and is much less negative inside that region. (Credit: Efthimios Kaxiras, *Atomic and Electronic Structure of Solids* (Cambridge University Press, 2003))[22]

1. Focus our attention only on the valence electron, which play a main role in physical properties of the crystal and live mostly far away from the core, in the calculation and ignore the core electrons which always gather around the nucleus and is not important in determining the crystal properties. We will take the effect of core electron into account only through their screening of the nucleus potential.

2. As shown in the right panel of Fig. 3.1, replace the original nuclueus potential $\tilde{V}^{nuc}$ by the pseudopotential $\tilde{V}^{ion}$ which matches $\tilde{V}^{nuc}$ outside certain distance from the core and is much less negative than $\tilde{V}^{nuc}$ inside that threshold distance.

In this way, we need not consider the highly oscillating core electrons and the valance electron is much less oscillating in the region close to the nuclues. The calculation can be speeded up greatly because there is less electron needed to be concerned and we can set a much lower energy cutoff E_{cut} (or crystal momentum cutoff $\vec{K}_{max}$) after getting rid of the highly oscillating component. These simplications are reasonable because chemistry happens

in the region far away from the nucleus core and it is the valence orbitals which determine the chemical reactivity of the crystal and how the crystal response to the applied electromagnetic fields in various spectroscopy. This method for simplifying the calculation is known as the pseudopoential method.

Chapter 4

Experimental Results

4.1 Methods

We performed scanning tunneling microscope (STM) measurement using a home-built STM at liquid helium temperature (∼4-5K) to study Sb.

The Sb sample used was prepared by Dillon Gardner and Yong Lee in MIT. It is from a high-purity antimony (99.999%, supplied by Alfa Aesar®) in shot form (10.15 g, 6 mm) which was sealed in an evacuated quartz tube, and heated in a box furnace to 700°C for 24 hours. The furnace was then cooled slowly (0.1°C/min) to 500°C, and subsequently cooled to room temperature.

Before being inserted into the STM, single crystals of Sb were cleaved in-situ in cryogenic ultrahigh-vacuum to expose the (111) face. In the STM, a mechanically cut PtIr tip, cleaned by field emission and characterized on gold, was used for measurements. As introduced in a previous chapter, we acquired spectroscopy data by the lock-in technique at frequency $f = 1.115$ kHz and conductance maps by recording out-of-feedback dI/dV spectra at each spatial location.

4.2 Sb Structure in literature versus the topography in our experiment

The structure of Sb(111) is shown in Fig. 4.1(a), from which we can see that the inter-bilayer distance [23, 24] is 2.2 Å and the intra-bilayer length is 1.5 Å. Since the bonding is much stronger within the bilayer than that between the bilayer, when the sample is cleaved, it is typically cleaved between the bilayer. If there were any steps presented on the surface after the cleavage, the expected step height would be 2.2 Å + 1.5 Å = 3.7 Å.

In our STM experiment, we observed a topography of a cleaved Sb(111) surface like what Fig. 4.1(b) is showing. There are a number of steps on it and its height profile along the grey line is shown in Fig. 4.1(d). There are two types of step heights whose values are around 1.5 Å and 2.2 Å.

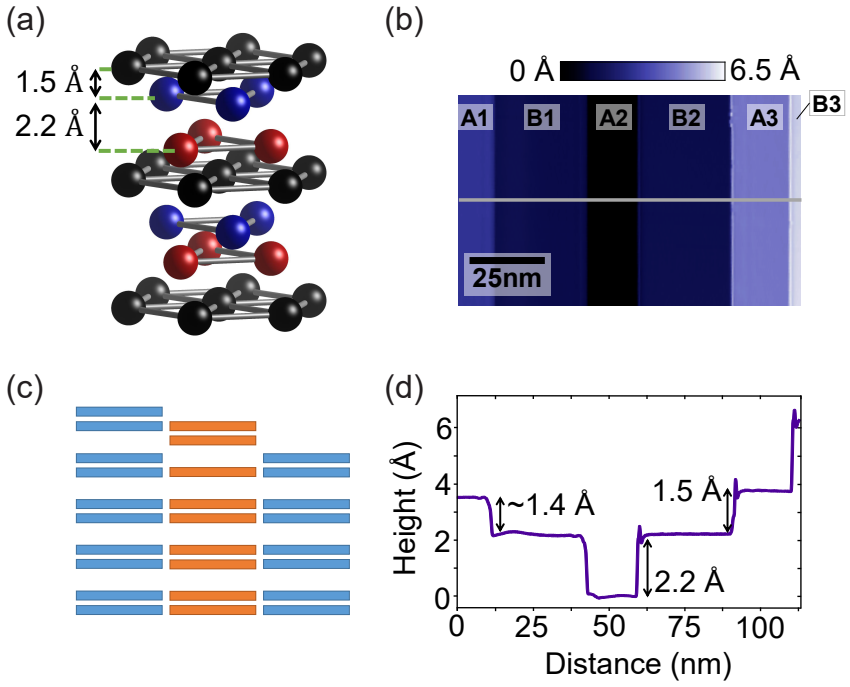

Figure 4.1: **Terraces Structures of Antimony. (a)** Bilayer crystal structure of Sb(111). Intrabilayer distance is 1.5 Å and interbilayer distance is 2.2 Å. **(b)** Topography of steps observed on Sb(111) by scanning tunneling microscope (STM). (sample bias, V_0=300mV; juction resistance, R_J=3 GΩ; resolution=70×1200 pixels) **(c)** A cartoon model showing how different step height observed can be formed using bilayers and a single broken layer of Sb. The blue terrace is called normal and the orange terrace with a single broken layer is called abnormal. **(d)** Height profile along the grey line in (b). From the step heights observed, it can be identified that B1, B2 and B3 in (b) are abnormal terraces.

They are much closer to the length of the intra- and inter- bilayer distance respectively than that of the usual expected step height (3.7 Å). These kinds of unusual step heights can be produced by the cartoon model in Fig. 4.1(c), where there is a single broken layer beneath the surface of a terrace (the orange terrace). In the following, we will call this kind of unusual terrace as 'abnormal terrace and the terrace without a single broken layer (the blue terrace) as a 'normal terrace. When the abnormal terrace is sandwiched between two normal terrace as in the model of Fig. 4.1(c), the step heights between the normal and abnormal terraces on the left and right ends would correspond to the intra- and inter- bilayer distances respectively. It should also be noted that the unusual step heights can be obtained no matter the single broken layer is located on the first bilayer (i.e. on the surface) or several bilayers below the surface. From the height profile in Fig. 4.1(d), we can see that terrace B1 and B2 in Fig. 4.1(b) could be identified as the abnormal terraces. The existing of the single broken layer can be due to the cleavage in our experiment or the imperfect of the sample.

4.3 dI/dV Spectra

4.3.1 Zero bias peak on abnormal surface

Fig. 4.2(a) is showing the averaged spectra on the surfaces of the normal and abnormal terraces in Fig. 4.1(b). Compared with the spectrum on the normal terrace, there is a characteristic peak at zero bias of width ∼13 meV (by a Lorentzian fit) on the abnormal terrace. A linecut along the grey line in Fig. 4.1(b) is obtained and the result is shown in Fig. 4.2(b), where the relative color is showing the relative intensity of dI/dV (thus the density of states). It can be seen that the zero bias peaks (ZBP) are quite robust on the abnormal terrace. Apart from that, there is a series of euqally spaced wiggling energy peaks in the dI/dV spectrum in Fig. 4.2(a) from -100 to 0 meV on both the normal and abnormal terrace. These wigglings will be explained in the next subsection.

4.3.2 Wiggling in the spectrum

The wigglings in spectra are also observed by Seo *et al.* [25] on their steps of Sb surface. This kind of quantized resonance are caused by the scattering of the surface states from the step edges, reflecting the reflection properties of those steps.

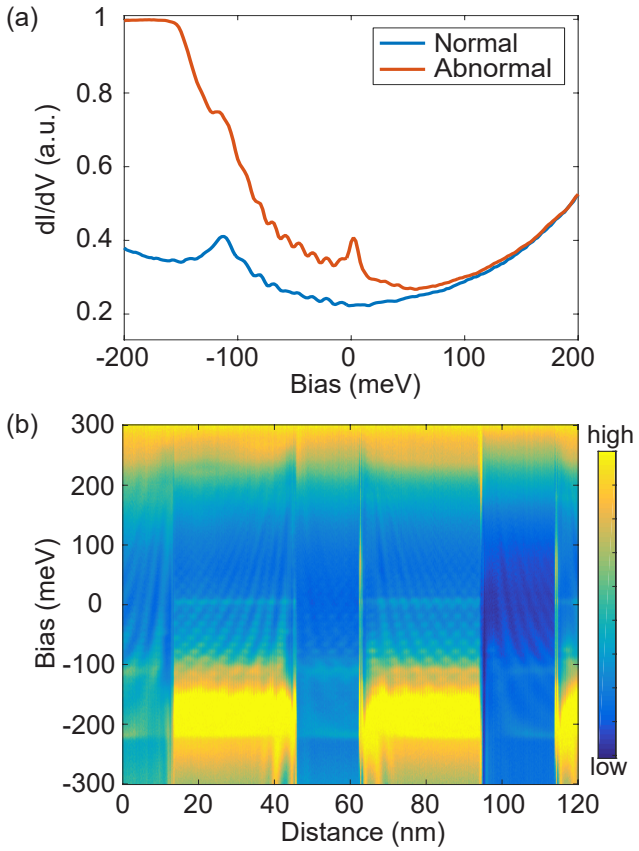

Figure 4.2: **dI/dV Spectra observed on different terraces. (a)** Averaged dI/dV spectra observed on the normal and abnormal terraces, featuring the zero bias conductance peak on the abnormal terrace. (V_0 = 300 mV; R_J = 300 MΩ; V_{rms} = 5 mV) The blue curve is from the normal terrace and the orange curve is from the abnormal terrace. They are averaged along the grey line on the A2 normal terrace and B1 abnormal terrace in Fig. 4.1(b) respectively. **(b)** A linecut of dI/dV spectra (arbitrary units) along the grey line in Fig. 4.1(b), normalized with respect to the maximum intenisty along the entire inecut, showing quasiparticle interference pattern. The color is the magnitude of the dI/dV spectrum. (V_0 = 300 mV; juction resistance, R_J = 300 MΩ; V_{rms} = 5 mV; obtained at 5.4K)

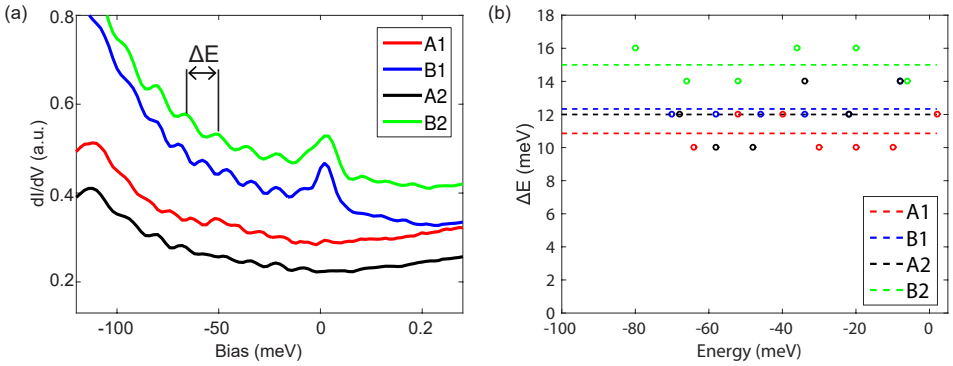

Figure 4.3: **Wigglings in dI/dV spectra on normal and abnormal surfaces and the energy difference between peaks (a)** Averaged dI/dV measurement on different surfaces featuring quantized peaks in energy ranging from -100 to 0 meV. ΔE is defined to be the energy difference between adjacent peaks. The speactra are offset vertically for clarity. (Obtained at 2 meV per energy point; $V_0 = 300$ mV; $R_J = 300$ MΩ; $V_{\text{rms}} = 5$ mV)**(b)** Energy spacing between quantized peaks in (a). Dotted lines are the avearges energy seperation.

As pointed out by Seo *et al.* [25], if scattering resonance is really the origin of the wigglings, the energy peaks should be equally spaced in the spectra. So we look more closely on the wigglings in Fig. 4.3(a) and plot out the energy spacing (ΔE) between different wiggling peaks on each spectrum in Fig. 4.3(b). Indeed, given the sampling rate of the dI/dV spectra was 2 meV per energy point and the lock-in V_{rms} amplitude is 5 meV, the energy spacing of the wiggling peaks shown in Fig. 4.3(b) is quite constant in every dI/dV spectra.

An immediate question would be: is the ZBP also caused by quantum resonance? On the abnormal steps B1 and B2, the average energy seperation between those peaks are 12.3 and 15 meV respectively. The energy difference between the ZBP and its closest wiggling peak are 10 and 8 meV on B1 and B2 respectively, which tend not to be in the trend of the equally spaced series of peaks. Also, the amplitude of the ZBP is much larger than those wigglings peak. Noticibly, there is also a wiggling peak at 0 meV on the normal surface A1. But the amplitude is similarly small as the other wiggling peaks on that surface. So it can be seen that the ZBP on the abnormal surface may not be due to the quantum resonance of the steps.

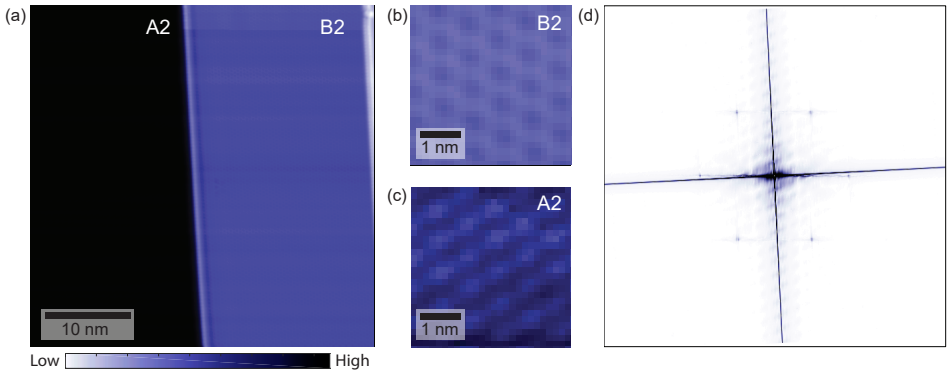

Figure 4.4: **STM Topography of the normal and abnormal steps and its Fourier transform (a)** STM Topography of the step with the normal surface A2 on the left side and abnormal surface B2 on the right side. The total field of view is 40×40 nm. (sample bias, V_0 = 300mV; juction resistance, R_J = 3 GΩ; resolution = 512×512 pixels) **(b,c)** Zoomed-in of (a) for the abnormal B2 (b) and normal A2 (c) steps showing atomic resolution. **(d)** Fourier transfrom of (a) from which we can see there is only one set of hexagonal Bragg peaks corresponding to the lattice constant of the surfaces. This reveals that there is no lattice constant change on the abnormal surface.

4.3.3 No superconductivity involved

In our experiment, only pristine Sb was used. There is no superconductivity proximity effect to induce the zero bias peak, although Wittig [26] pointed out that Sb can be superconducting with critical temperature 3.5 K at high pressure, because the temperature in our experiments were 4.5 K - 5.4 K. However, Reale [27] suggested that there is a metastate of Sb of a more densely packed face centered cubic structure with a much shorter lattice constant can have a critical temperature of as high as 7.5 K under huge strain and pressure. Therefore, we tried to compare the topography of the normal and abnormal surfaces in Fig. 4.4 and see if there is any change in the lattice constant.

In the metastate of Sb of FCC structure suggested by Reale [27], the distance between atoms in hexagonal pattern on the (111) surface would become about 3.2 Å, around 25% smaller than the usual distance, which is 4.3 Å[24]. This would give us a set of bragg peak in the fourier space with

1/3 larger magntitude corresponding to that shortened atomic distance.

So when we Fourier transform a topography having both the normal and abnormal surfaces, if the abnormal surface had a diffferent lattice constant as the normal surface, we would expect two sets of hexagonal Bragg peaks in the Fourier space, where one set corresponding to the altered lattice constant on abnormal surface has magnitude about 1/3 larger than the other set corresponding to the original lattice constant on the normal surface. However, as apparent in Fig. 4.4(d), there is only one set of hexagonal Bragg peak. This shows that there is no crystal structure change on the abnormal surface and thus there would not be potential for the abnormal surface to be superconducting at our operating temperature. In this way, we can verify that there is no superducting involved in the ZBP on the abnormal terrace.

4.4 Momentum resolved spectroscopic information

To clarify the origin of the zero bias peak on the abnormal terrace, we need to know more about the momentum-resolved spectroscopic information on this terrace. There are two ways STM can obtain this information, namely through quasiparticle interference (QPI) and Landau quantization. It has been showed that these two pieces of information can be obtained simultaneously [13].

4.4.1 Quasiparticle interference (QPI)

The surface state quasiparticle of Sb is scattered by the step on each terrace. The scattered outgoing surface states interfered with the incoming states to create interference pattern on terraces as shown in Fig. 4.2(b). This is known as QPI. The peaks in the Fourier transform of the interference patterns at different energy are corresponding to the possible scattering modes at that energy, which in turn reflect the band structure of the terrace. The band structure of the normal terrace of Sb is well-studied [13] and from that we know the surface state of Sb that can be probed by QPI is from about -250 meV to about 100 meV. So we Fourier transformed the interference pattern of the line-cuts in Fig. 4.2(b) for the normal and abnormal terraces respectively. Fig. 4.5(a) is showing the results for the normal terrace along the Γ-M direction. There are two noticeable linear dispersions starting from around -200 meV and -100 meV. It agrees with what [13] has shown and they are corresponding to the two scattering modes in the double cone of

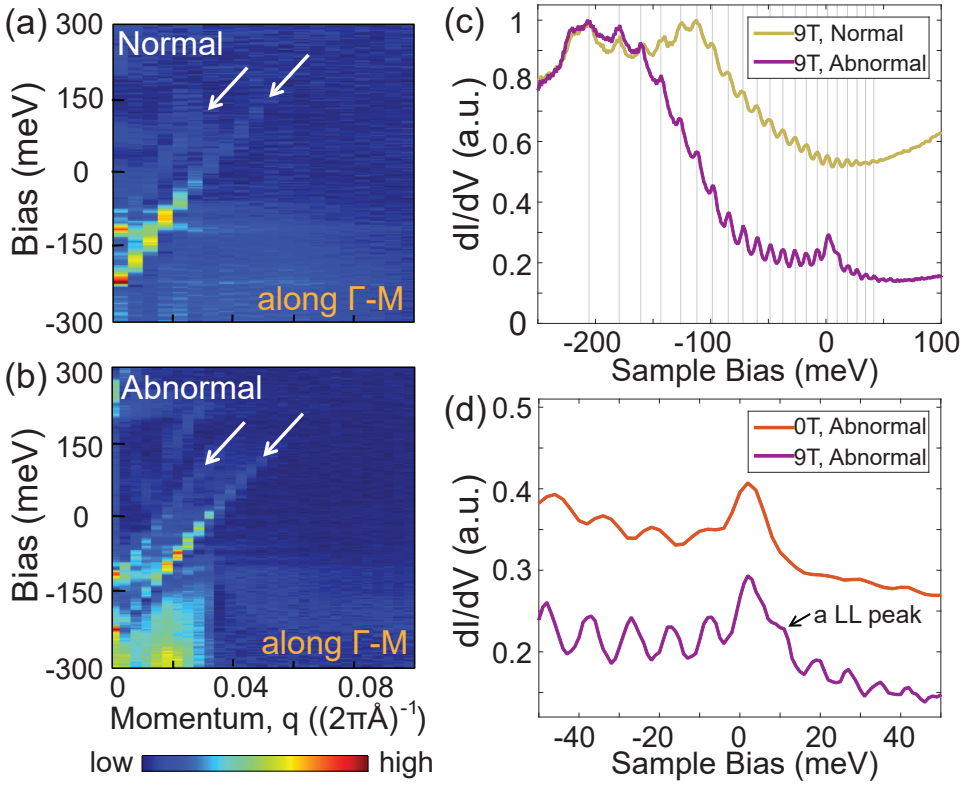

Figure 4.5: **Dispersing modes from Quasiparticle Interference and Landau Quantization of surface states.** **(a,b)** Representative 1D Fourier Transforms (arbitrary unit) of the quasiparticle interference in the dI/dV linecuts of normal (a) and abnormal (b) in Fig. 4.2(b), showing two similar prominent dispersing modes along the Γ-M direction. Each graph has intensity relative to itself. **(c)** Comparison of dI/dV spectra at magnetic field B=9T on the abnormal terrace (purple line, $V_0 = 300$mV; juction resistance, $R_J = 300$ MΩ; $V_{\text{rms}} = 1$ mV; obtained at 4.5K) and normal terrace (the yellowish brown line). Both curves are normalized with respect to themselevs. The pale grey lines behind the curves are comparing the energy position of different Landau level peaks on the two curves, demonstrating those peaks are at the same energy values on the normal and abnormal terraces. **(d)** Zoomed-in comparison of the zero bias conductance peaks on abnormal terrace in magnetic field 9T (the purple line, obatined at 4.5K) and out of field (the orange line, obatined at 5.4K). We can see that the zero bias peak is still quite robust in magnetic field.

the surface states of Sb. Fig. 4.5(b) is showing dispersion of the QPI on the abnormal terrace. Similar to the normal terrace, there are two linear dispersing modes starting from about −200 meV and −100 meV. This shows that the main features of the surface states of the abnormal terrace should be quite similar to that of the normal terrace.

4.4.2 Landau levels

The other phenomena that can reflect the band structure is Landau levels (LL) in the dI/dV spectrum. Applying strong magnetic field (>4 T) to the Sb sample can cause conductance oscillation in the DOS spectrum and they are known as the LL peaks. As in other topological materials, we can interpret the LLs in the Dirac fermion picture [28–31]. The energy of the n^{th} LL increases with $\sqrt{nB}$. The Bohr-Sommerfeld quantization relation suggests the momentum space radius for the n^{th} LL orbit is also proportional to $\sqrt{nB}$ [28]. So, by tracing the energy of the n^{th} peak in the DOS spectrum, we can deduce the dispersion of the energy of surface states versus momentum. In other words, the energy location of the LL peaks is reflecting the band structures. Fig. 4.5(c) is comparing the LL peaks on the normal Sb from [13] in magnetic field of 9T (the yellowish brown curve) and the peaks on the abnormal terrace of Sb in our experiment in the same strength of magnetic field (the purple curve). As indicated by the grey lines in the background, the energy of the peaks in both curves match quite well with each other. This also suggests that the band structure of the surface states on the abnormal terrace are quite similar to that on the normal terrace. Fig. 4.5(d) is demonstrating that in the presence of magnetic field of 9T, the zero bias peak is still robust, showing no clear evidence of peak splitting, for its width remains to be about 10 meV by the Lorentzian fit. Thus the possibility for Kondo effect [12, 32] to play a role in inducing the ZBCP is not apparent from the experiment

Chapter 5

DFT Results

To gain theoretical insight into the origin of the ZBP, density functional theory (DFT) simulation was carried out to compare the calculated band structure of the abnormal terrace and the normal terrace.

5.1 Methods

The DFT calculation was performed using the Vienna *ab initio* simulation package (VASP) code[33–35], with the projector augmented plane wave method. The exchange-correlation energy is estimated by the Perdew-Burke-Ernzerhof (PBE) functional and the energy cutoff for the plane-wave basis function is 300 eV. A Γ-ceneterd k-point mesh of (21,21,1) was used in the crystal structural relaxation while a much finer k-point mesh of (200,200,1) was used in the band structure calculation.

The band structures and surface states of the normal and abnormal terraces were simulated from a slab geometry. Ideally, the larger the slab (i.e. the more layers in the slab) is, the more reliable will be the results because the less influenzed by the finite size effect. So we included a slab as large as possible until we hit the limit of our calculating power. Eventually, a normal slab of 46 layers and an abnormal slab of 47 layers (with an extra single broken layer) were used.

In the structural optimization of the abnormal terrace, we first put the single broken layer at the surface of the slab and allow it to relax. After relaxation of the layers, the single broken layer sunk into the bulk of the slab. It indicates that in experiment, even if the single broken layer was created at the surface accidentally when we cleaved the sample in situ, the crystal would relax and other layers would rearrange themselves so that the single broken layer would appear below the surface in order to lower the energy. So we put the single broken layer at different depth below the surface, allowed it to relax and calculated the band structure. We found that the broken layer would continue to fall to the lower layer until we put it more than 4 bilayers below the surface. So we will focus on band structure calculated

from abnormal slab with a single broken layer more than 4 layers below the surface.

Also, noticing in STM experiments, electronic states on the surface are mainly concerned because they are what mostly the tip can probe. So the bands available at the surface of the slab would be the most of our interest. Furthermore, the outermost valence electrons in Sb are in s and p orbitals. Since the p_z orbital is pointing out of the page and much more far reaching than the s orbital to the tip, it would be the closest to the tip in STM and dominate the measurement in experiment. Hence, to recognize the main contributor in experiment and to compare what happened on the surfaces of the normal and abnormal terrace, we projected the available electronic states in p_z orbital on the surface in the band structure. In Fig. 5.1 and Fig. A.1 showing the calculated band structures, the greys lines would be the unavailable states on the surface and the available states are colored according to their normalized relative contribution to the DOS spectrum.

5.2 Band structure of normal and abnormal terrace

5.2.1 Normal surface

The calculated band structure of the normal terrace along the M-K-Γ-M direction is plotted in Fig. 5.1(a). As in literature [13], the surface state for the normal surface of Sb is a double Dirac cone ranging from around -250 meV to 100 meV. There is a saddle point (ϵ_s) at around -0.1 eV. The energy of the minimum of the cones (ϵ_B) are a bit above -300 meV and that of an extreme ϵ_T is just above 0.2 eV. The shapes and main features of the calculated band structure for normal terrace agree quite well with the other publication [13]. The subtle difference in the exact value could be due to the finite size of the slab.

5.2.2 Abnormal surface

Fig. 5.1(b) is showing the typical result for the abnormal terrace, in which a slab of 47 layers with the single broken layer 6 bilayers (or 12 layers) below the surface had been used.

As implied by [36], the contribution of states in momentum space to the DOS spectrum will decay away from the Γ point exponentially. So we could focus at the band structure around the Γ point as zoomed in Fig. 5.1(c) and

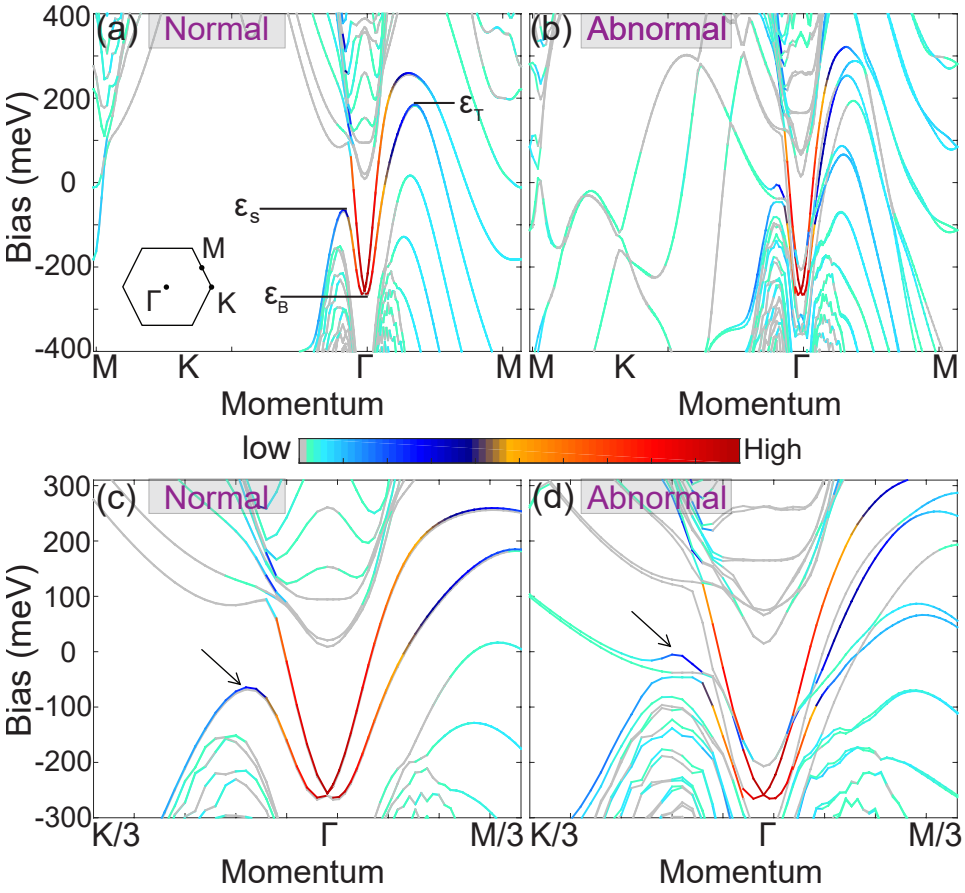

Figure 5.1: **Band Structure of normal and abnormal terraces. (a,b)** Band Structure of the normal (a) and abnormal (b) terrace from density functional theory (DFT). The color intenisty is the projection of the relative amount of available states of p_z orbital on the surfaces. The grey lines are the unavailable states on the surfaces. **(c,d)** Zoomed in of the band structures of the normal (c) and abnormal (d) surfaces around the Γ point. The saddle points are indicated by the arrows.

(d) for the normal and abnormal surfaces. From Fig. 5.1(d), the double-cone feature of the surface state is preserved on the abnormal terrace. It is still lying in the similar range of energy as in the normal terrace case if we compare Fig. 5.1(c) and (d). This explains why similar QPI and Landau quantization, which reflect the characteristics of the surface state, were observed on the abnormal terrace in our experiment.

Now we may turn our attention to the saddle point causing the zero bias conductance peak. As mentioned above, on the normal terrace, there is a saddle point (ϵ_s) around -0.1 eV on the outer cone along the Γ-K direction. By [13], this saddle point causes a peak at around -0.1 eV in the DOS spectrum of the normal terrace. However, on the abnormal terrace (Fig. 5.1(e)), there are more states appearing below this saddle point, pushing it up to the Fermi energy (0 eV). This will constitute a van Hove singularity leading to a peak in the zero bias of the DOS spectrum. This pused-up saddle point can be seen in slabs with the single broken layer at different depths (as long as it can be stabilized). Other plots of band structure for the abnormal terrace with slab of different thickness and single broken layer at different depth can be found in Appendix A. A justification of DFT results by comparing with experimental data is also included in Appendix B. Our findings suggested that the origin of the zero bias peak observed in experiment is just due to the abrupt change of the crystal and is trivial.

Other characteristics in the DOS spectrum of the abnormal terrace from Fig. 4.2(a) included a larger bump at negative energies from -200 meV to 0 meV, compared with that of the normal terrace. Comparing the band structures of the normal (Fig. 5.1(c)) and abnormal (Fig. 5.1(d)) terraces, there are more available states on the abnormal terrace around the Γ point from around -200 meV to 0 meV. This naturally explains why the dI/dV conductance is enhanced on the abnormal terrace from -200 meV to 0 meV.

5.2.3 Further investigation for magnetic breakdown

The increased number of states on the abnormal terrace in the concerned energy range from -200 meV to 200 meV may have another implication. Energy of Landau level is determined by the area enclosed by the state in momentum space. On the abnormal terrace, when there are more states at the same energy, they collide and interfere with the original state in the momentum space with an example shown in Fig. 5.2(a-b). (The evolution of the crossing is shown more clearly in Fig.5.2(c-h).) Hybridization between the newly emergent states and the original states would happen. The area enclosed by the original state could be affected. In this way, the Landau

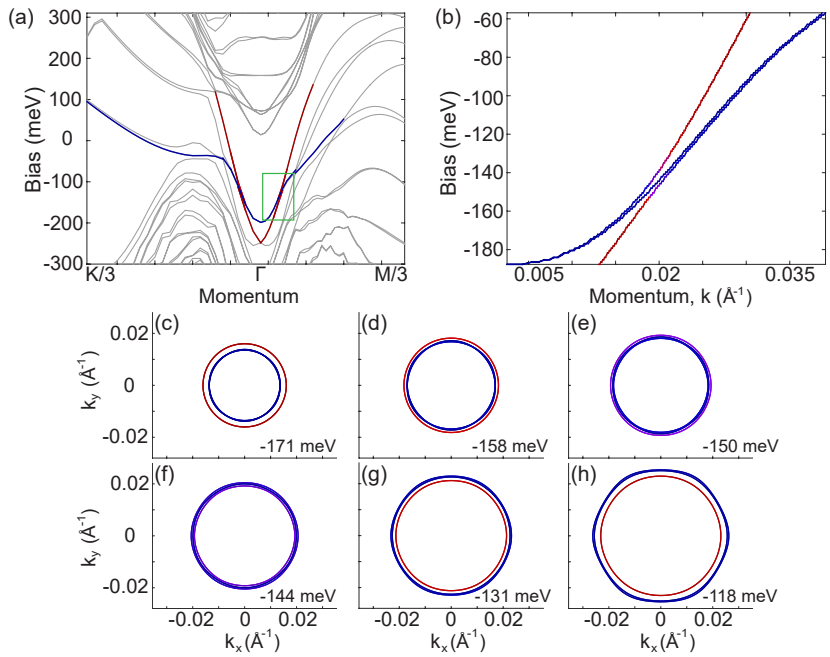

Figure 5.2: **Extra emergent band on the abnormal terrace cutting across the Dirac cone (a,b)** (a) Band structure on the abnormal surface from DFT (data from thickness 47 (depth 6) is employed). The red curve is representing the inner Dirac cone and the blue curve is the emergent band cutting cross the Dirac cone. Other states not being concenred here are in grey. The portion along the Γ-M direction enclosed in the green box in (a) is enlarged in (b). **(c-h)** Energy contour of the inner cone (red) and the emergent band (blue) from energies below to above the crossing.

levels should be changed. However, from our experiment, the Landau levels was not altered by that. This problem is known as 'magnetic breakdown' [37]. It was proposed that electrons could jump across the hybridized orbital and remain in the original way of motion. Further investigation can be conducted to establish a more satisfactory and complete explanation for that.

Chapter 6

Conclusion

We reported that zero bias conductance peak, which can be a signature of Majorana fermion, would be possibly resulted from an abrupt change of a topological material, Sb, with a trivial origin.

The ZBP happens on the abnormal terrace of Sb, with a single broken layer beneath the surface. Using STM, we found that the QPI and LLs on the abnormal surface are similar to that on the normal surface. Then we simulated the band structures of those two kinds of surfaces by DFT. It reveals that both the normal and abnormal terraces have a similar double cone surface states, which provide an explanation for the similar QPI and LLs observed by STM. However, on the abnormal terrace, there is a saddle point around the Γ point being pushed up to energy ~ 0 meV which could a zero bias peak in dI/dV spectrum due to van Hove singularity.

The lesson learnt is that when we are trying to probe Majorana fermion in the interface of a topological insulator and a superconductor, even if we are not working with Sb, we should make sure the signal is not trivially from the crystal itself.

In addition, more complete mechanism can be sought to describe why there is magnetic breakdown when extra state is introduced to interfere with the original states.

Bibliography

[1] Sergey Bravyi and Alexei Kitaev. Fermionic quantum computation.

[2] Sergey Bravyi. Universal quantum computation with the ν=52 fractional quantum Hall state. *Phys. Rev. A*, 73(4):042313, 2006.

[3] Jason Alicea, Yuval Oreg, Gil Refael, Felix von Oppen, and Matthew P. a. Fisher. Non-Abelian statistics and topological quantum information processing in 1D wire networks. *Nat. Phys.*, 7(5):412–417, 2011.

[4] Liang Fu and C L Kane. Superconducting Proximity Effect and Majorana Fermions at the Surface of a Topological Insulator. *Phys. Rev. Lett.*, 100(March):096407, 2008.

[5] K. T. Law, Patrick A. Lee, and T. K. Ng. Majorana Fermion Induced Resonant Andreev Reflection. *Phys. Rev. Lett.*, 103(23):237001, 2009.

[6] A. R. Akhmerov, J. P. Dahlhaus, F. Hassler, M. Wimmer, and C. W J Beenakker. Quantized conductance at the majorana phase transition in a disordered superconducting wire. *Phys. Rev. Lett.*, 106(5):057001, 2011.

[7] M. T. Deng, C. L. Yu, G. Y. Huang, M. Larsson, P. Caroff, and H. Q. Xu. Anomalous zero-bias conductance peak in a Nb-InSb nanowire-Nb hybrid device. *Nano Lett.*, 12(12):6414–6419, 2012.

[8] V. Mourik, K. Zuo, S. M. Frolov, S. R. Plissard, E. P. a. M. Bakkers, and L. P. Kouwenhoven. Signatures of Majorana Fermions in. *Sci.*, 336(6084):1003, 2012.

[9] Anindya Das, Yuval Ronen, Yonatan Most, Yuval Oreg, Moty Heiblum, and Hadas Shtrikman. Zero-bias peaks and splitting in an Al-InAs nanowire topological superconductor as a signature of Majorana fermions. *Nat. Phys.*, 8(12):887–895, 2012.

[10] Jin Peng Xu, Mei Xiao Wang, Zhi Long Liu, Jian Feng Ge, Xiaojun Yang, Canhua Liu, Zhu An Xu, Dandan Guan, Chun Lei Gao, Dong Qian, Ying Liu, Qiang Hua Wang, Fu Chun Zhang, Qi Kun Xue, and Jin Feng Jia. Experimental detection of a Majorana mode in the core of a magnetic vortex inside a topological insulator-superconductor Bi2Te3/NbSe2 heterostructure. *Phys. Rev. Lett.*, 114(1):017001, 2015.

[11] Jie Liu, Andrew C Potter, K T Law, and Patrick A Lee. Zero-Bias Peaks in the Tunneling Conductance of Spin-Orbit-Coupled Superconducting Wires with and without Majorana End-States. *Phys. Rev. Lett.*, 109(December):267002, 2012.

[12] Sungjae Cho, Ruidan Zhong, John A Schneeloch, Genda Gu, and Nadya Mason. Kondo-like zero-bias conductance anomaly in a three-dimensional topological insulator nanowire. *Sci. Rep.*, 6(October 2015):21767, 2016.

[13] Anjan Soumyanarayanan, Michael M Yee, Yang He, Hsin Lin, Dillon R Gardner, Arun Bansil, Young S Lee, and Jennifer E Hoffman. Momentum-resolved STM studies of Rashba-split surface states on the topological semimetal Sb. *J. Electron. Spectrosc. Relat. Phenom.*, 201:66–73, 2015.

[14] Guanggeng Yao, Ziyu Luo, Feng Pan, Wentao Xu, Yuan Ping Feng, and Xue-Sen Wang. Evolution of Topological Surface States in Antimony Ultra-Thin Films. *Sci. Rep.*, 3:02010, 2013.

[15] Jihwey Park, Yeong-Ah Soh, Gabriel Aeppli, Xiao Feng, Yunbo Ou, Ke He, and Qi-Kun Xue. Crystallinity of tellurium capping and epitaxy of ferromagnetic topological insulator films on SrTiO3. *Sci. Rep.*, 5(February):11595, 2015.

[16] Pedram Roushan, Jungpil Seo, Colin V Parker, Y S Hor, D Hsieh, Dong Qian, Anthony Richardella, M Z Hasan, R J Cava, and Ali Yazdani. Topological surface states protected from backscattering by chiral spin texture. *Nature*, 460(7259):1106–1109, 2009.

[17] Haim Beidenkopf, Pedram Roushan, Jungpil Seo, Lindsay Gorman, Ilya Drozdov, Yew San Hor, R. J. Cava, and Ali Yazdani. Spatial fluctuations of helical Dirac fermions on the surface of topological insulators. *Nat. Phys.*, 7(12):939–943, 2011.

[18] P. Hohenberg and W. Kohn. Inhomogeneous electron gas. *Phys. Rev. Lett.*, 136(3B):864–871, 1964.

[19] W. Kohn and L. J. Sham. Self-consistent equations including exchange and correlation effects. *Phys. Rev.*, 140(4A), 1965.

[20] John P. Perdew and Yue Wang. Accurate and simple analytic representation of the electron-gas correlation energy. *Phys. Rev. B*, 45(23):13244–13249, 1992.

[21] John P. Perdew, Kieron Burke, and Matthias Ernzerhof. Generalized Gradient Approximation Made Simple. *Phys. Rev. Lett.*, 77(18):3865–3868, 1996.

[22] Efthimios Kaxiras. *Atomic and Electronic Structure of Solids*. Cambridge University Press, 2003.

[23] C. S. Barrett, P. Cucka, and K. Haefner. The crystal structure of antimony at 4.2, 78 and 298 K. *Acta Crystallogr.*, 16(6):451–453, 1963.

[24] Yi Liu and Roland E. Allen. Electronic Structure of. *Phys. Rev. B*, 20(7):1566–1577, 1995.

[25] Jungpil Seo, Pedram Roushan, Haim Beidenkopf, Y S Hor, R J Cava, and Ali Yazdani. Transmission of topological surface states through surface barriers. *Nature*, 466(7304):343–346, 2010.

[26] J. Wittig. A study of the superconductivity of antimony under pressure and a search for superconductivity in arsenic. *J. Phys. Chem. Solids*, 30(6):1407–1410, 1969.

[27] C. Reale. Properties of vapour-quenched superconducting A1-type As, Sb and Bi films. *Vacuum*, 28(1):1–3, 1978.

[28] T Hanaguri, K Igarashi, M Kawamura, H Takagi, and T Sasagawa. Momentum-resolved Landau-level spectroscopy of Dirac surface state in Bi 2 Se 3. *Phys. Rev. B*, 105:081305, 2010.

[29] Yoshinori Okada, Chetan Dhital, Wenwen Zhou, Erik D Huemiller, Hsin Lin, S Basak, A Bansil, Y Huang, H Ding, Z Wang, Stephen D Wilson, and V Madhavan. Direct Observation of Broken Time-Reversal Symmetry on the Surface of a Magnetically Doped Topological Insulator. *Phys. Rev. Lett.*, 106(May):206805, 2011.

[30] Peng Cheng, Canli Song, Tong Zhang, Yanyi Zhang, Yilin Wang, Jinfeng Jia, Jing Wang, Yayu Wang, Bang-fen Zhu, Xi Chen, Xucun Ma, Ke He, Lili Wang, Xi Dai, Zhong Fang, Xincheng Xie, and Xiao-liang Qi. Landau Quantization of Topological Surface States in Bi 2 Se 3. *Phys. Rev. Lett.*, 105(August):076801, 2010.

[31] Yeping Jiang, Yilin Wang, Mu Chen, Zhi Li, Canli Song, Ke He, Lili Wang, Xi Chen, Xucun Ma, and Qi Kun Xue. Landau quantization and the thickness limit of topological insulator thin films of Sb 2Te 3. *Phys. Rev. Lett.*, 108(1):016401, 2012.

[32] Pengbin Niu, Yun-Long Shi, Zhu Sun, Yi-Hang Nie, and Hong-Gang Luo. Kondo peak splitting and Kondo dip induced by a local moment. *Sci. Rep.*, 5:18021, 2015.

[33] G. Kresse and J. Hafner. Ab initio molecular dynamics for liquid metals. *Phys. Rev. B*, 47(1):558–561, 1993.

[34] G. Kresse and J. Furthmüller. Efficient iterative schemes for ab initio total-energy calculations using a plane-wave basis set. *Phys. Rev. B*, 54(16):11169–11186, 1996.

[35] G. Kresse and J. Furthmüller. Efficiency of ab-initio total energy calculations for metals and semiconductors using a plane-wave basis set. *Comput. Mater. Sci.*, 6(1):15–50, 1996.

[36] J Tersoff and Dr Hamann. Theory and application for the scanning tunneling microscope. *Phys. Rev. Lett.*, 50(25):1998–2001, 1983.

[37] D Shoenberg. *Magnetic Oscillation in Metals*. Cambride University Press, 1984.

Appendix A

Band Structures of different thickness and depth

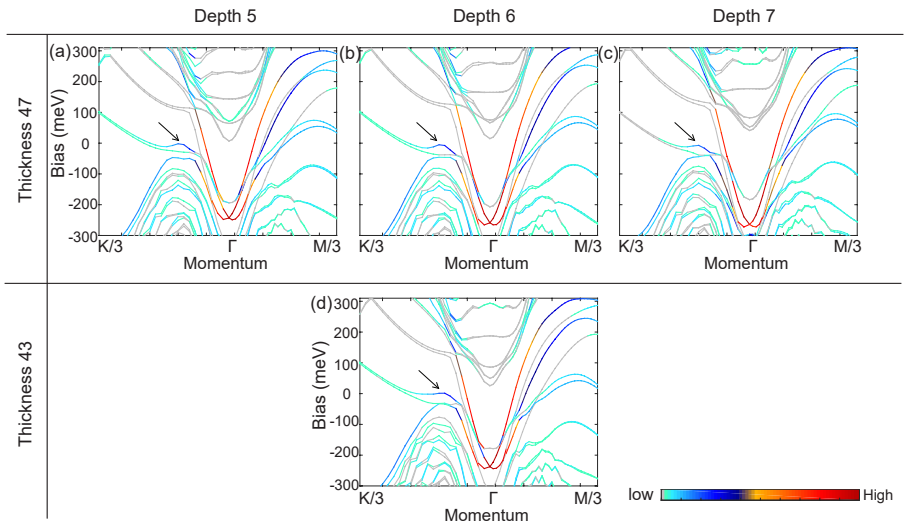

Figure A.1: **Band structures from DFT with different thickness and depth of the single broken layer (a-c)** Band structures from DFT using slabs with 47 total layers and single broken layer at depth 5 (a), 6 (b) and 7 (c). They all have a saddle point (indicated by the black arrow) around 0 meV. **(d)** Band structure from a slab with different thickness (43 layers in total) and single broken layer at depth 6. Ideally the larger the slab, the smaller the finite size effect and the more reliable is the calculation. (And 47 total layers is the limit of our computational resources.) But comparing (b) and (d), we can still identify similar main features of the band structures of the abnormal surfaces, especially the saddle point around 0 meV.

Appendix B

Justification of Validity of DFT calculation

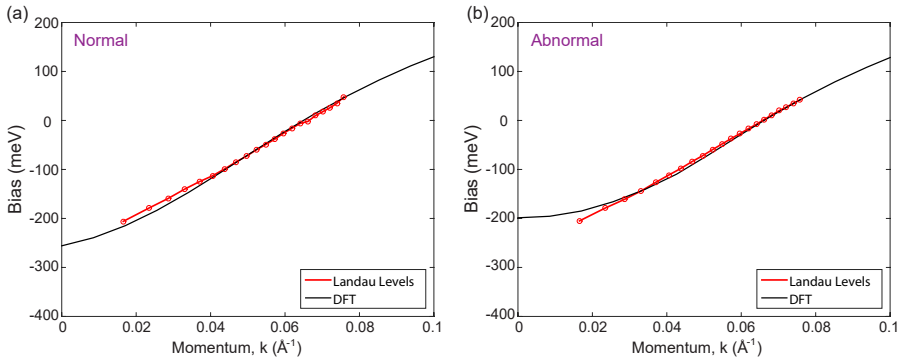

Figure B.1: **Comparison of Band Structure infered from Landau levels in dI/dV spectrum and that from DFT (a,b)** Using the semiclassical Bohr-Sommerfeld quantization relation [28], the inner cone in the band structure can be deduced from the energies of Landau level peak in the dI/dV spectrum. Red curves in the above figures are showing the inner cones calculated from Landau levels on the normal (a) and abnormal (b) terraces. The inner cone from DFT (black curves, data from thickness 47 (depth 6) is employed) are also drawn in the figures. It can be seen that DFT match quite well with the experimental data, especially from -100 meV to 0 meV in which the semiclassical approximation for Landau levels is particularly reliable. This comparison can be regarded as a test for the validity of the DFT results.